AD_____

Award Number: W81XWH-04-1-0481

TITLE: High Resolution X-Ray Phase Contrast Imaging with Acoustic Tissue-Selective Contrast Enhancement

PRINCIPAL INVESTIGATOR: Gerald J. Diebold, Ph.D.

CONTRACTING ORGANIZATION: Brown University
Providence, RI 02912

REPORT DATE: June 2005

TYPE OF REPORT: Annual

PREPARED FOR: U.S. Army Medical Research and Materiel Command
Fort Detrick, Maryland 21702-5012

REPORT DOCUMENTATION PAGE

Form Approved
OMB No. 0704-0188

1. REPORT DATE *(DD-MM-YYYY)*	2. REPORT TYPE	3. DATES COVERED *(From - To)*
01-06-2005	Annual	1 Jun 2004 – 31 May 2005

4. TITLE AND SUBTITLE
High Resolution X-Ray Phase Contrast Imaging with Acoustic Tissue-Selective Contrast Enhancement

5a. CONTRACT NUMBER

5b. GRANT NUMBER
W81XWH-04-1-0481

5c. PROGRAM ELEMENT NUMBER

6. AUTHOR(S)
Gerald J. Diebold, Ph.D.

E-mail: Gerald_diebold@brown.edu

5d. PROJECT NUMBER

5e. TASK NUMBER

5f. WORK UNIT NUMBER

7. PERFORMING ORGANIZATION NAME(S) AND ADDRESS(ES)
Brown University
Providence, RI 02912

8. PERFORMING ORGANIZATION REPORT NUMBER

9. SPONSORING / MONITORING AGENCY NAME(S) AND ADDRESS(ES)
U.S. Army Medical Research and Materiel Command
Fort Detrick, Maryland 21702-5012

10. SPONSOR/MONITOR'S ACRONYM(S)

11. SPONSOR/MONITOR'S REPORT NUMBER(S)

12. DISTRIBUTION / AVAILABILITY STATEMENT
Approved for Public Release; Distribution Unlimited

13. SUPPLEMENTARY NOTES

14. ABSTRACT

We show that ultrasound can be used for contrast enhancement in high-resolution x-ray imaging of tissue and soft materials. Interfacial features of objects are highlighted as a result of both the displacement introduced by the ultrasound and the inherent sensitivity of x-ray phase contrast imaging to density variations. We have performed preliminary theoretical calculations of the radiation force induced by a sound fields and compared it to our experimental results. Some further characteristics of the method are demonstrated by imaging Teflon beads embedded in agarose. Additionally, we have developed the theoretical and experimental tools required to perform tomography using acoustically modulated X-ray phase contrast imaging. Some preliminary 3D tests reported.
We are now ready to perform the first 2D and 3D measurements of biological samples using acoustically modulated X-ray phase contrast imaging.

15. SUBJECT TERMS
x-ray, ultrasound, phase contrast, imaging, elastography

16. SECURITY CLASSIFICATION OF:			17. LIMITATION OF ABSTRACT	18. NUMBER OF PAGES	19a. NAME OF RESPONSIBLE PERSON
a. REPORT	b. ABSTRACT	c. THIS PAGE			19b. TELEPHONE NUMBER *(include area code)*
U	U	U	UU	17	

Table of Contents

Introduction

Phase contrast imaging differs from conventional x-ray shadowgraphy in the mechanism of contrast generation: while conventional shadowgraphy depends on absorption of x-rays, phase contrast imaging is based on phase changes as x-rays traverse a body resulting in wave interference that result in intensity changes in the image. The complex index of refraction n for any material is given by

$$n = 1 - \delta - i\beta \qquad (1)$$

where the imaginary part β of the index describes x-ray absorption and the real part δ describes the phase shift undergone by the x-radiation as it passes through a material. Fresnel-Huygens theory [1-3], which governs image formation in general, describes contrast in an image as dependent on both absorption and phase contrast. However, only when sources with high spatial coherence, such as synchrotrons [4-6], microfocus x-ray tubes [7], or laser plasma x-ray sources [8,9]are employed is the phase contrast component of the image visible. Coherent sources give an image of a dense object embedded in lower density, soft tissue as a shadow of the object, caused by absorption, surrounded at its perimeter by light and dark interference fringes arising from rapid phase variations in the radiation at the interface between the two media.

A detailed analysis of the relative contrast produced in an image for a fixed difference in density shows that phase contrast is more sensitive than absorption throughout most of the spectral region commonly used for diagnostic x-ray imaging[10]. For instance, the thickness of water needed to produce a 1% phase-contrast at 36-keV photon energy is 2500 times smaller than that required to produce the same contrast though absorption[10].

Phase contrast in an image can be markedly enhanced by recording two images of an object, one where the object is displaced slightly through acoustic radiation pressure[11], and a second where the object is unmoved, followed by subtraction of the two images. Acoustic radiation forces can arise from either reflection of sound by an object or as a result of acoustic impedance changes (*i.e.* a variation in either density or sound speed) or by dissipative processes within the object resulting in absorption of the ultrasound energy [12]. A number of studies[13-18] have shown that soft tissue can be manipulated by ultrasonic pressure. Typically, a mechanical actuator or a beam of ultrasound moves an object whose position is monitored in time with conventional pulse-echo ultrasonic imaging. It has been shown that variations in Young's modulus, which, in part, determines sound speed, permits acoustic differentiation of tissue. It is known, for instance, that breast tumors have a significantly different Young's modulus from surrounding tissue, and that tumors move as rigid bodies in response to acoustic radiation pressure [14,16-19]. Intense ultrasound is used to exert forces on objects within a body giving displacements on the order of tens to hundreds of microns. Subtraction of images made with and without the ultrasound field gives an image that removes low spatial frequency features and highlights high frequency features. The method acts as an acoustic "contrast agent" for phase contrast x-ray imaging, which in soft tissue, acts to highlight small density changes. We have named this method acoustically modulated X-ray phase contrast.

We report here some preliminary experimental and theoretical studies of acoustic radiation pressure. We have also performed some additional proof of concept type experiments combining ultrasound and X-ray phase contrast. Finally, we are also developing the software and hardware necessary to perform tomographic studies; some first theoretical and experimental tests have been completed.

Body

Acoustic Radiation Pressure

For the purposes of the present study, where reflection of the acoustic wave is considered, it can be said that for a fixed acoustic impedance change, the force exerted by an ultrasonic wave is proportional to the time average of the energy density of the wave and the area of the object presented to the sound field. An expression for the acoustic radiation force on an arbitrary object has been given by Westervelt [11] and evaluated for spheres small compared with the wavelength of the radiation. For spheres of any diameter, King [20] has given an expression that agrees with the limiting expression given by Westervelt. According to King, the average acoustic radiation force exerted on a sphere of radius a is given by:

$$\bar{F}_{ac} = \frac{2\pi \cdot p^2}{(ka)^2 k^2 c^2 \rho} \cdot A(ka) \qquad (2)$$

where ρ and c are the density and speed of sound of the medium, respectively, p is the acoustic pressure, k is the wave number of the radiation, and A(ka) is given by

$$A(ka) = \frac{1}{H_0 H_1} + \frac{2}{H_1 H_2}\left\{\frac{\left[(ka)^2 - 3\left(1 - \frac{\rho}{\rho_S}\right)\right]^2}{(ka)^8}\right\} + \sum_{n=2}^{\infty}\left(\frac{(n+1)}{H_n H_{n+1}} \frac{\left((ka)^2 - n(n+1)\right)^2}{(ka)^{4(n+1)}}\right) \qquad (3)$$

where the functions H_n for small ka are given by

$n = 0:$

$$H_0 = \frac{\left(1+(ka)^2\right)}{(ka)^2}$$

$n = 1:$

$$H_1 = \frac{4}{(ka)^6}\left(\left(1+\frac{\rho}{2\rho_s}\right)^2 + \frac{(ka)^2}{2}\left(1+\frac{\rho}{2\rho_s}\right)^2\frac{\rho}{\rho_s} + \frac{(ka)^4}{4}\right)$$

$n = 2:$

$$H_2 = \frac{81}{(ka)^{10}}\left(1+\frac{(ka)^2}{10} - \frac{2(ka)^2}{81} + \frac{(ka)^6}{81}\right)$$

$n > 2:$

$$H_n = \frac{(n+1)^2\left(\prod_{i=1}^{n}(2n-1)\right)^2}{(ka)^{4n+2}}\left(1+\frac{n-1}{(n+1)(2n-1)}(ka)^2+\ldots\right)$$

where ρ is the density of the fluid and ρ_s is the density of the sphere. For $ka > 2$, the functions H_n are given by

$n = 0:$

$$H_0 = \frac{\left(1+(ka)^2\right)}{(ka)^2}$$

$n = 1:$

$$H_1 = \frac{\pi}{2(ka)^3}\left(\left(1-\frac{\rho}{\rho_s}\right)^2\left(J_{\frac{3}{2}}^2 + J_{-\frac{3}{2}}^2\right) + 2ka\left(1-\frac{\rho}{\rho_s}\right)\left(J_{-\frac{3}{2}}J_{-\frac{5}{2}} + J_{\frac{3}{2}}J_{\frac{5}{2}}\right) + (ka)^2\left(J_{\frac{5}{2}}^2 + J_{-\frac{5}{2}}^2\right)\right)$$

$n > 1:$

$$H_n = \frac{\pi}{2(ka)^{2n+1}}\left(n^2\left(J_{n+\frac{1}{2}}^2 + J_{-n-\frac{1}{2}}^2\right) + 2ka\left(J_{-n-\frac{1}{2}}J_{-n-\frac{3}{2}} + J_{n+\frac{1}{2}}J_{n+\frac{3}{2}}\right) + (ka)^2\left(J_{n+\frac{3}{2}}^2 + J_{-n-\frac{3}{2}}^2\right)\right)$$

where J_n is a Bessel function of order n, and were the argument of each of the Bessel functions is ka.

Figure 1 is a plot of force versus ka from Eq. 2, with the inset showing a portion of the curve for small ka. The parameters used in Eq. 2 were for a Teflon bead with a = 1.5 mm, $\rho/\rho_s = 2$; and for water with $c = 1500$ m/s and $\rho = 10^3$ kg/m^3. The curves in Figure 1 show a steady increase in the force with increasing ka

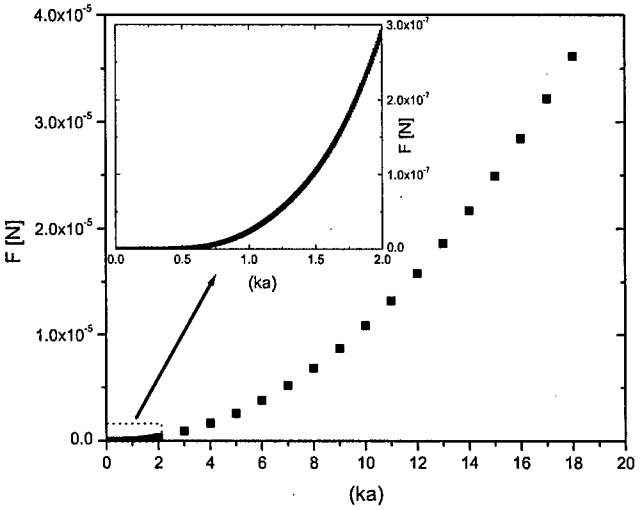

Figure 1: Radiation force (in N) versus *ka* (dimensionless) from Eq. 6. Inset: Magnified view of the first part of the curve. The portions of the curves for $ka<2$ were calculated using the small *ka* expressions for the functions H_n.

Experiments were carried out to determine the deflection of a Teflon bead in water using an x-ray imaging apparatus to determine the deflection of the bead as a function of acoustic pressure. The x-rays, generated by a microfocus x-ray tube (Oxford Ultrabright Microfocus UB-M1), were directed onto a sample cell consisting of a 3-cm diameter PVC tube which had portions machined out and replaced with Mylar foil to reduce x-ray intensity losses. The x-ray beam, as shown in Fig. 2, propagated through a He filled tube to a Gd2O2S(Tb) fiber optic scintillation plate (Hamamatsu, Inc. Model J6676) the fluorescence from which was imaged onto a liquid nitrogen cooled CCD camera (Roper Scientific Model 7382-0001). The intensity maximum of the emission x-ray spectrum was 40 keV. The source-to-detector distance was 2.6 m, while the sample-to-source distance was 0.35 m, giving a magnification of 7.5 and a maximum phase contrast for spatial frequencies corresponding to 4.3 μm.

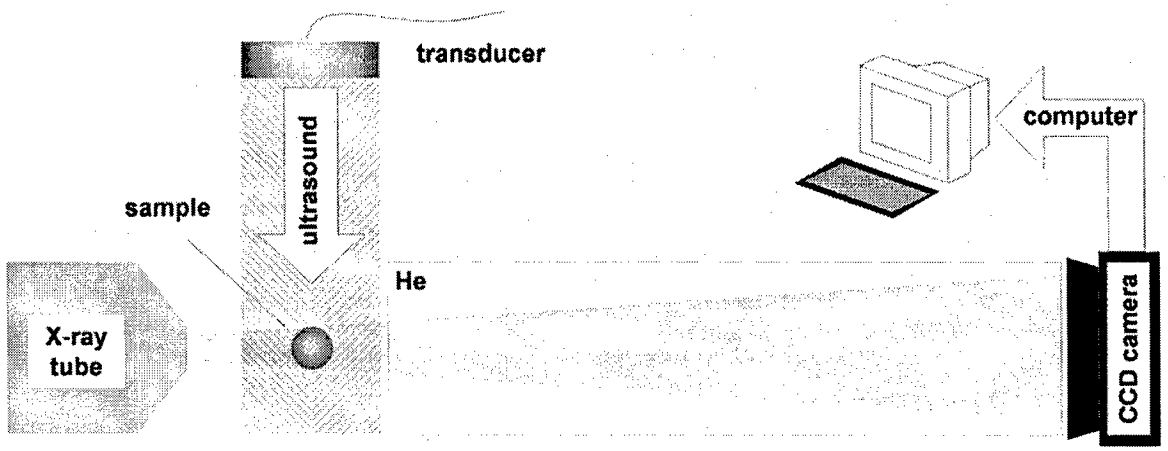

Figure 2: Diagram of the experimental apparatus. X-radiation generated by a microfocus tube penetrates a sample and is detected by a CCD camera that views a scintillation plate. The CCD camera is read by the computer which stores the images and performs the subtractions.

The acoustic transducer used to produce radiation pressure was a 1 MHz, $LiNbO_3$-transducer located 3 cm from the bead. One end of the PVC sample tube was terminated by a synthetic, sound-absorbing plastic. The pulse train from the function generator (Agilent Model 33250A) used to drive the transducer consisted of 15-μs bursts at a repetition rate of 133 Hz. The signal from the function generator was amplified by a power amplifier with a peak output power of 1.5 kW and delivered to the transducer. Although the low duty cycle of the pulse sequence, approximately 0.2%, resulted in a reduced time average acoustic power from the transducer, the resulting radiation pressure was sufficient to cause displacements that could be easily imaged with the CCD camera. A 3 mm diameter Teflon bead was attached to a glass fiber and suspended in the center of the sample cell, which was filled with water. The glass fiber was calibrated by attaching it to a precision translation stage and using a laboratory balance to determine force versus fiber displacement. The data shown in Fig. 3(A) gave a force constant of 2.18×10^{-2} N/m for the fiber. The total force on a bead suspended from the fiber is the sum of the restoring force from the fiber and the force from gravity, which can be written for small angles of deviation from the vertical as

$$F_{exp} = F_{\text{glassfiber}} + \frac{m_{\text{bead}} \cdot g \cdot d}{L} \qquad (4)$$

where m_{bead} is the mass of the bead, g is the gravitational constant, L is the length of the fiber and d is its displacement. For the experiments described here, the mass of the bead was 35 mg, and the length of the glass fiber was 10 cm. The displacement of the bead versus the time averaged electrical power delivered to the transducer is shown in Fig. 3 (B). The break in the slope of the curve can be attributed to a departure of the efficiency of the transducer from linearity at high driving voltages. The acoustic pressure generated

by the transducer at various power levels from the power amplifier was determined using a calibrated $LiNiO_3$ transducer (LaserSonics Technologies, Model WAT-04). The plot of acoustic pressure from the calibrated transducer versus average driving voltage applied to the transducer is shown in Fig. 4(A) which gives a curve with the same qualitative features as the curve in Fig. 3(B), and permits calibration of the transducer pressure in terms of the power amplifier output driving voltage. With this calibration, the plot in Fig. 3(B) can be converted to a plot of force versus the square of the acoustic pressure as shown in Fig. 4(B). The theoretical curve from Eq. 6, also plotted in Fig 4(B), shows reasonably good agreement with the experimental measurements. The maximum force recorded in the experiments was 5 μN.

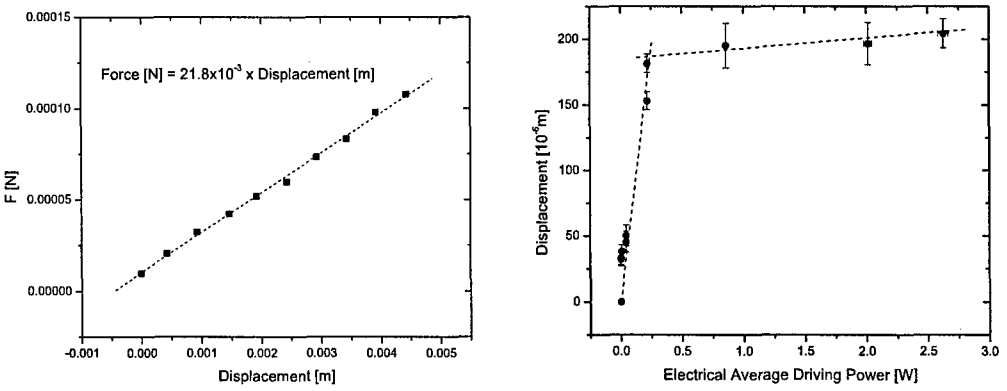

Figure 3: (A) Force on the glass fiber in *N* versus displacement in *m*. (B) Displacement of the Teflon bead attached to the fiber versus average electrical power delivered to the transducer.

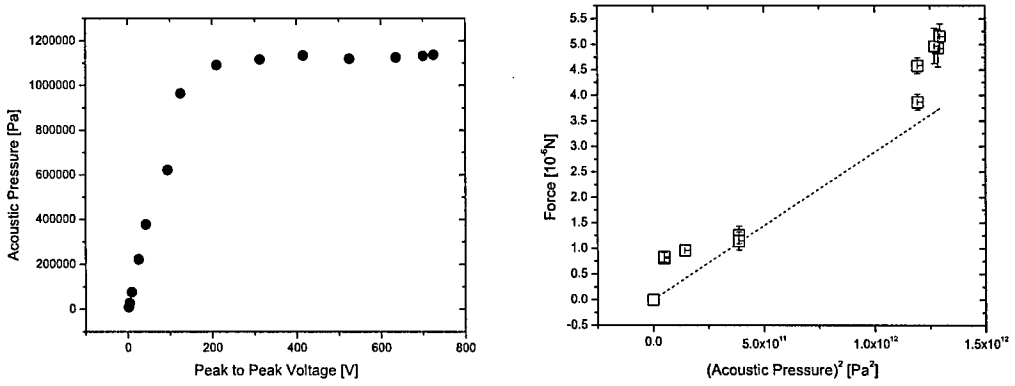

Figure 4: (A) Acoustic pressure in *Pa* from the calibrated transducer versus driving voltage from the power amplifier. (B) Force on the bead in *N* versus the square of the pressure from the transducer.

Acoustically Modulated X-ray Phase Contrast Imaging

The method of modifying a phase contrast image using acoustic radiation pressure [21,22] consists of two steps: first, an x-ray image is made with a sound beam directed into a body to displace an object through acoustic radiation force and the image stored in a computer, second, another x-ray image is of the object is taken, this time without the presence of the sound beam and the image is recorded in the computer. The two images are then subtracted pixel by pixel to give a subtracted phase contrast image, the component of the image from absorption contrast being largely eliminated, leaving a nearly pure phase contrast image, inherently background and flatfield corrected.

The principle of the method was demonstrated by taking images of two 3-mm diameter Teflon beads cast in a 6.5-cm long block of agarose. As shown in Fig. 5 (A), the two beads were both within the field of the x-ray beam, but only one bead was irradiated with ultrasound. Figure 5 (B) shows an image of the two beads where the microfocus x-ray tube was operated at high power, 80 W, to enlarge the diameter of the x-ray source to approximately 75 μm. With this source diameter, the phase contrast component of the image disappears as a result of convolution of the phase contrast fringes over the source area of the x-ray beam. The exposure time for the image was 75 s. In Fig. 5 (C) a conventional phase contrast image of the two beads is shown using the same total x-ray fluence as was used in Fig. 5 (B), but with the x-ray tube operating at 10 W, where source diameter was 25 μm. The fringes at the perimeters of the beads, which serve to define the edges of the beads, are the result of interference from rapid phase variations in the x-ray paths, which, for a sphere, are largest at its perimeter [23]. The results of the image subtraction with the ultrasound directed onto only the bead closest to the x-ray tube are shown in Fig 5 (D). The bead that was not irradiated with ultrasound is not visible in the image, while the phase contrast component of the image of the irradiated bead shows up with the phase contrast component highlighted. The subtracted phase contrast image in Fig. 5 (D) shows a reversal of the bright and dark regions at the perimeter of the bead in the direction of the ultrasound at the two sides of the bead (which appear at the top and bottom of Fig. 5 (D)): the interior of the arc at the top of the figure appears bright while it

is the exterior of the arc at the bottom of the figure that appears bright. The reversal of the shading is a consequence of subtraction — the opposite shading could be produced by reversal of the order of subtraction of the two images.

As a result of a collaboration with the Brown Medical School, we will soon be able to test our technique on biological samples. We will obtain mouse skin and liver tumors. The first measurements are expected to corroborate our preliminary proof of concept experiments.

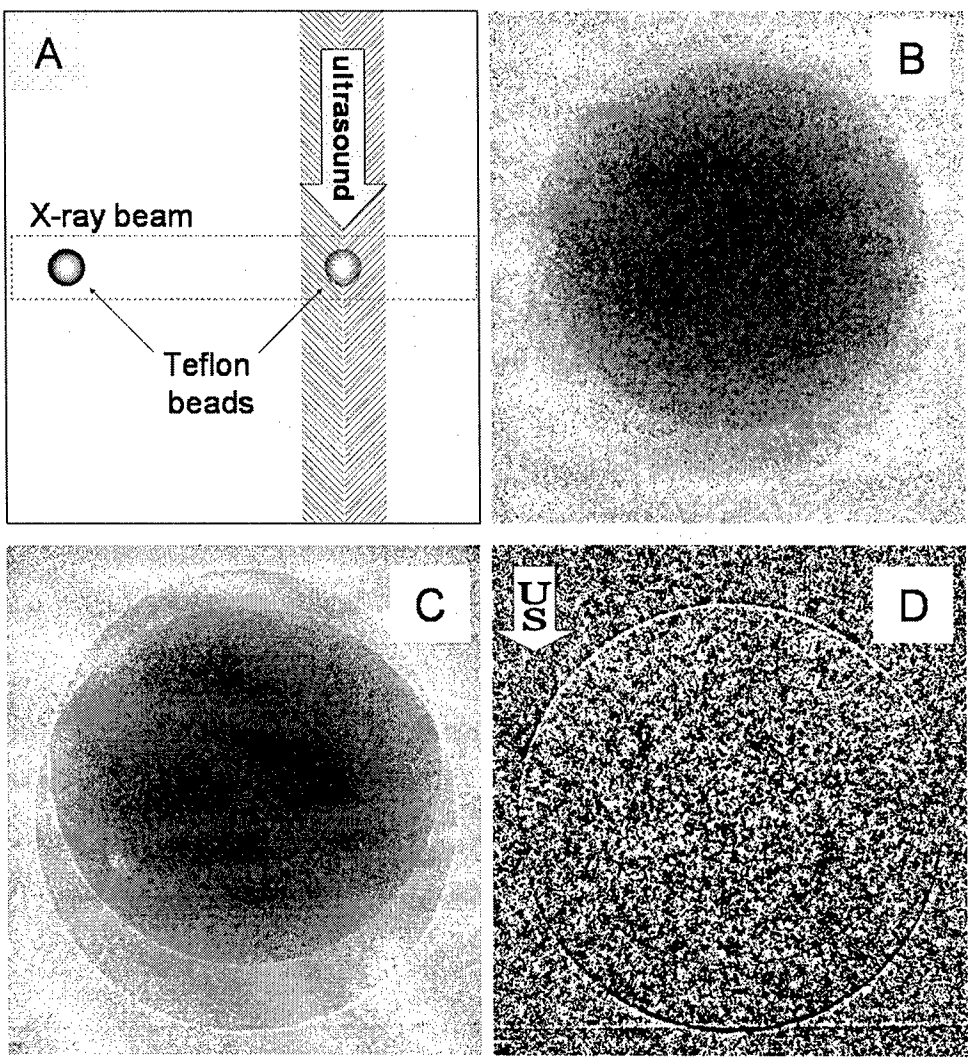

Figure 5: (A) Side view of the sample consisting of two Teflon beads cast in agarose. The two beads are separated by 3 cm. (B) Image of the beads with no phase contrast. (C) Image of the beads with phase contrast. (D) Subtracted image of the two beads. The bead irradiated with ultrasound is nearest the CCD camera and produces a slightly larger image than the bead located outside the sound beam. The x-ray tube voltage for the images was 90 kV. The image in (B) was taken with a 75 s exposure time with the x-ray tube operating at 80 W; the image in (C) was taken with eight times lower tube wattage and eight times longer exposure to give the same total x-ray fluence.

X-ray Phase Contrast Tomography

Tomographic back projection calculations provide the reconstruction of a 2D object from a serie of 1D projections [24]. If an object is described by the function f(x,y), the projection p(θ,r) of the object at a defined angle θ and at a distance r can be written as the Radon transform:

$$p(\theta,r) = Radon(f(x,y)) = \int_{-\infty}^{\infty}\int_{-\infty}^{\infty} f(x,y)\cdot\delta(x\cdot\cos\theta + y\sin\theta - r)dxdy$$

We want to recreate the object f(x,y) knowing the projections p(θ,r), namely applying an inverse Radon transform:

$$f(x,y) = Radon^{-1}(Proj(x,y)) = \frac{1}{2\pi}\int_{0}^{\pi}\int_{-\infty}^{\infty}\frac{\frac{1}{\pi}\frac{\partial}{\partial r}Projection(x,y)}{x\cdot\cos\theta + y\sin\theta - r}drd\theta$$

If all the projections are known, one could theoretically reconstruct the object. However, the inverse Radon equation is undefined when:

$r = x\cdot\cos\theta + y\sin\theta$

Practically, the filtered back projection algorithm is used to compute the inverse Radon transform. We used Matlab 7 to simulate and reconstruct defined objects. The filter is designed directly in the frequency domain and then multiplied by the FFT of the projections. The projections are zero-padded to a power of 2 before filtering to prevent spatial domain aliasing and to speed up the FFT.

The Radon transform can be used to describe a parallel beam geometry as shown in Figure 6A. Our experiment approximates a point source with a fan beam geometry as shown in Fig. 6B. We have computed our simulation transforming our fan beam data into a parallel beam geometry using Matlab 7 and then employing the Radon and inverse Radon functions.

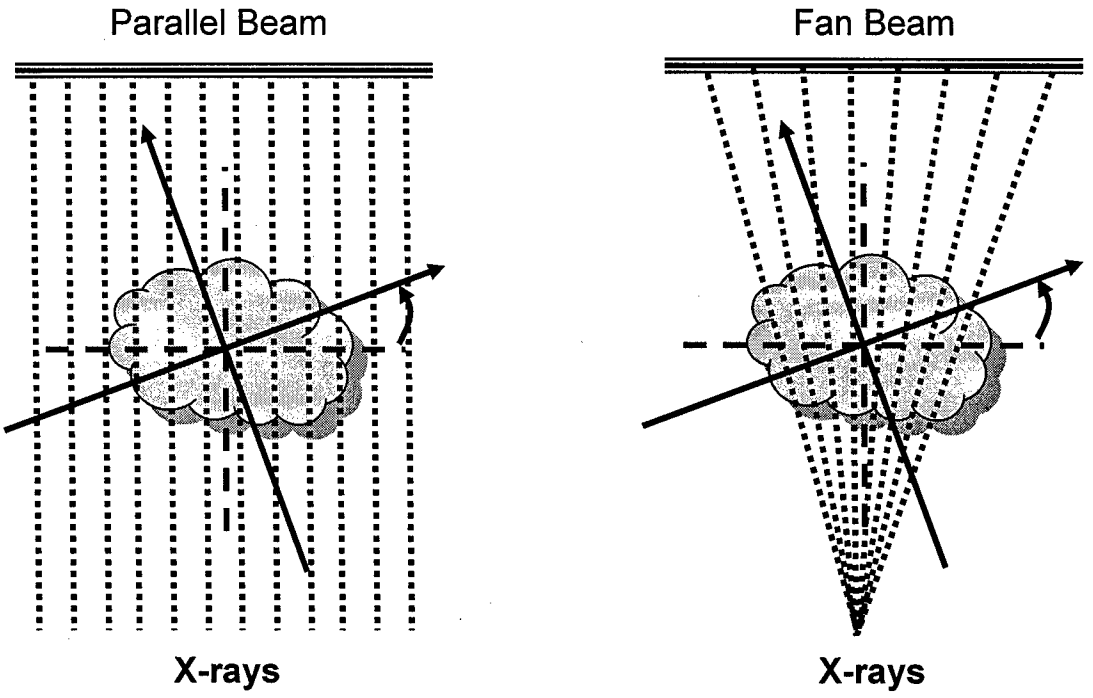

Figure 6: Schematic of the typical tomography geometries, (A) parallel beam and (B) fan beam case.

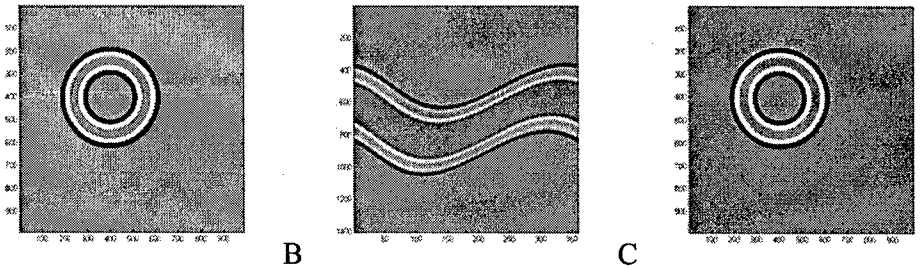

Figure 7: (A) Numerically simulated phase contrast signal of a hollow disc of low absorbing material. The expected Fresnel fringes have been reduced to just one dark and one light. The x-ray source is on the left. The axis of rotation is at position (500;500). (B) shows the fan beam projection of object (A). The X axis is now the angle value and the Y axis is the projected Y axis of the object on the detection plane. (C) shows the back projected object.

As a preliminary test, we have numerically simulated the phase contrast signal of a well defined phase object. A hollow disc of low absorbing material will generate a phase contrast signal as seen in Figure 7A. This represents a slice of a 3D object along the Z axis. The expected Fresnel fringes have been reduced to just one dark and one light ring. The x-ray source is on the left and the axis of rotation is at position (500;500). The projection shows the projected intensities of the object on the detection plane. The scheme is as follow, from a 2D object, one obtains 1D projections at defined angles. These 1D projections are put together in Figure 7B. This matrix is then used to reconstruct the original object using the filtered back projection algorithm, Figure7C. The reconstructed object is clearly in agreement with the original projected object.

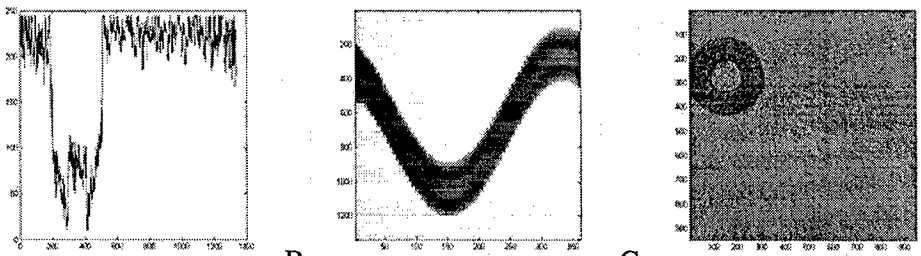

A B C

Figure 8: (A) shows a projection at a defined high and angle of a Teflon tube. (B) shows the fan beam projection of a Teflon tube. The X axis is the angle value and the Y axis is the distance on the detector. We measured at 5 degree increment. (C) shows the reconstructed object using the back projection algorithm.

We have developed an experimental setup to perform 3D measurements and as a first test, we have measured a standing Teflon tube. This sample gives a comparable signal to the simulated hollow disc of low absorbing material, Fig. 7A. Figure 8A shows a projection at a defined height and angle of the Teflon tube. By rotating the sample, we obtained the projection matrix, Figure 8B. Our algorithm reconstructs 2D objects from 1D projections. In the case of a 3D object, the typical procedure is to perform the reconstruction separately at different heights (z axis) and put the 2D together to obtain the final reconstructed 3D object. Such a 2D reconstruction is shown in Figure 8C. The angle increment of 5 degrees is responsible for some discrimination noise on the finale picture. We can now combine the reconstructed 2D objects in the z direction and obtain a series of cross sections of our object.

In the future, our tomographic setup will be used in combination with the acoustically modulated X-ray phase contrast imaging technique. Some interesting 3D pictures of ideal objects will be obtained; later, biological samples will be systematically investigated.

Key Research Accomplishments

We have demonstrated the effects of an acoustic field on a sphere in a fluid. Furthermore, we have performed comparative experimental measurements of a Teflon bead in water. We have been able to predict successfully the radiation force on the Teflon bead in water.

We have solidified our understanding and our technique by performing some additional proof of concept experiments. That is, we have shown that an object is selectively displaced by the sound field and not by secondary collective surroundings surface or volume effects.

We have demonstrated the ability to reconstruct 3D object using filtered back projection algorithm.

Reportable Outcomes

Best Paper Award in "Photons plus Ultrasound: Imaging and Sensing", International Society of Optical Engineering, SPIE given by Fairway Medical Technologies and LaserSonix Technologies, San Jose, California, 2005, to be published.

A. Beveridge, C. J. Bailat, T. J. Hamilton, S. Wang, C. Rose-Petruck, G. J. Diebold and V. Gusev, Imaging with Vibration Potential and Phase-contrast X-rays (accepted for publication)

T. J. Hamilton, C. J. Bailat, C. Rose-Petruck, G. J. Diebold, Acoustically Modulated X-ray Phase Contrast Imaging, Phys. Med. Biol., 49 (2004) 4985-4996.

C. J. Bailat, T. J. Hamilton, C. Rose-Petruck, G. J. Diebold, Acoustic radiation pressure: a phase contrast agent for x-ray phase contrast imaging, Appl. Phys. Lett., Vol. 85 No. 19, Nov. 2004, 4517-4519.

Conclusions

We have completed all the necessary construction of experimental apparatus and proven the concept of ultrasonically modified x-ray phase contrast imaging. We have shown the method has the ability to select objects within a body for imaging. We have laid the foundation for a new phase contrast tomography with ultrasonic radiation pressure.

References

1. Born, M. & Wolf, E. *Principles of Optics* (ed. Press, P.) (Pergamon Press, Oxford, England, 1980).
2. Cowley, J. M. (ed.) *Electron Diffraction* (Kluwer Academic Publishers, Dordrecht, 1991).
3. Cowley, J. M. *Diffraction Physics* (North Holland Physics Publishing, a division of Elsevier Science Publishers B.V., Amsterdam, 1984).
4. A Snigirev, I. S., V Kohn, S Kuznetsov, I Schelokov. On The Possibility of X-ray Phase Contrast Microimaging by Coherent High-energy Synchrotron Radiation. *Rev. Sci. Instr.* **66**, 5486 (1995).
5. Fulvia Arfelli, V. B., Alberto Bravin, Giovanni Cantatore, Edoardo Castelli et al. Mammography with Synchrotron Radiation: Phase Detection Techniques. *Radiology* **215**, 286-293 (2000).
6. Momose, A. Demonstration of phase-contrast x-ray computed tomography using an x-ray interferometer. *Nuclear Instruments & Methods in Physics Research, Section A: Accelerators, Spectrometers, Detectors, and Associated Equipment* **352**, 622-8 (1995).
7. Pogany, A., Gao, D. & Wilkins, S. W. Contrast and resolution in imaging with microfocus x-ray source. *Rev. Sci. Instr.* **68**, 2774 (1997).
8. Krol, A. et al. Laser-based microfocused x-ray source for mammography: Feasibility study. *Medical Physics* **24**, 725-732 (1997).
9. Krol, A., Kieffer, J. C. & Forster, E. Laser-driven x-ray source for diagnostic radiology. *Proceedings of SPIE-The International Society for Optical Engineering* **3157**, 156-163 (1997).
10. Beckmann, F., Bonse, U., Busch, F. & Gunnewig, O. X-ray microtomography (microCT) using phase contrast for the investigation of organic matter. *Journal of Computer Assisted Tomography* **21**, 539-53 (1997).
11. Westervelt, P. The Theory of steady Forces Caused by Sound Waves. *J. Acoust. Soc. Am.* **23**, 312 (1951).
12. Morse, P. M. *Vibration and Sound* (ed. Physics, A. I. o.) (Acoustical Society of America, 1981).
13. Muthupillai, R. et al. Magnetic resonance elastography by direct visualization of propagating acoustic strain waves. *Science (Washington, D. C.)* **269**, 1854-7 (1995).
14. Gao, L., Parker, K. J., Lerner, R. M. & Levinson, S. F. Imaging of the elastic properties of tissue--a review. *Ultrasound in Medicine and Biology* **22**, 959-77 (1996).
15. Fatemi, M. & Greenleaf, J. F. Ultrasound-stimulated vibro-acoustic spectrography. *Science* **280**, 82-5 (1998).
16. Nightingale, K., Nightingale, R., Palmeri, M. & Trahey, G. in *IEEE Ultrasonics Symp* 1319 (1999).
17. Sarvazyan, A. P. Shear Wave Elasticity Imaging: A New Ultrasonic Technology of Medical Diagnostics. *Ultrasound in Medicine and Biology* **24**, 1419 (1998).
18. McAleavey, S. A. Estimates of Echo Correlation and Measurement Bias in Acoustic Radiation Force Impulse Imaging. *IEEE Transactions on Ultrasonics, Ferroelectrics and Frequency Control* **50**, 631 (2003).

19. Nightingale, K., Stutz, D., Bentley, R. & Trahey, G. in *IEEE Symp* 525 (2002).
20. King, L. V. On the Acoustic Radiation Pressure on Spheres. *Proceedings of the Royal Society of London, Series A, Mathematical and Physical Sciences* **147**, 212-240 (1934).
21. C. J. Bailat, T. Hamilton, Rose-Petruck, C. & Diebold, G. J. Acoustic radiation pressure: a phase contrast agent for x-ray phase contrast imaging. *Appl. Phys. Lett.* **85**, 4517-4519 (2004).
22. T. Hamilton, C. J. Bailat, Rose-Petruck, C. & Diebold, G. J. Acoustically Modulated X-ray Phase Contrast Imaging. *Phys Med Biol* **49**, 4985-4996 (2004).
23. Wilkins, S. W., Gureyev, T. E., Gao, D., Pogany, A. & Stevenson, A. W. Phase-contrast imaging using polychromatic hard x-rays. *Nature* **384**, 335-338 (1996).
24. Radon, J. Über die Bestimmung von Funktionen durch Integralwerte längs gewisser Mannigfaltigkeiten, Berichte Sächsische Akademie der Wissenschaften. *Math.-Phys. Kl.* **69**, 262-267 (1917).